J. Fluid Mech. (2007), *vol.* 583, *pp.* 99–122.
doi:10.1017/S0022112007006155 Printed in the United Kingdom

Large-eddy simulations of gas-turbine swirl injector flow dynamics

SHANWU WANG,[1] VIGOR YANG[1]†, GEORGE HSIAO,[2] SHIH-YANG HSIEH[2] AND HUKAM C. MONGIA[2]

[1]Department of Mechanical and Nuclear Engineering, The Pennsylvania State University, University Park, PA 16802, USA

[2]GE Aviation, Cincinnati, OH 45215, USA

(Received 29 July 2005 and in revised form 30 January 2007)

A comprehensive study on confined swirling flows in an operational gas-turbine injector was performed by means of large-eddy simulations. The formulation was based on the Favre-filtered conservation equations and a modified Smagorinsky treatment of subgrid-scale motions. The model was then numerically solved by means of a preconditioned density-based finite-volume approach. Calculated mean velocities and turbulence properties show good agreement with experimental data obtained from the laser-Doppler velocimetry measurements. Various aspects of the swirling flow development (such as the central recirculating flow, precessing vortex core and Kelvin–Helmholtz instability) were explored in detail. Both co- and counter-rotating configurations were considered, and the effects of swirl direction on flow characteristics were examined. The flow evolution inside the injector is dictated mainly by the air delivered through the primary swirler. The impact of the secondary swirler appears to be limited.

1. Introduction

Swirl injectors have been widely adopted for modern gas-turbine engine combustors (Lefebvre 1999) and other energy-conversion systems for propulsion and power-generation applications (Bazarov, Yang & Puri 2004). Devices of this kind have evolved over the past four decades and have matured to deliver stable, efficient and clean combustion. In the past, empirical design methodologies were commonly implemented in the development of gas-turbine combustors to evaluate the performance and emission characteristics of production hardware (Mongia 1998; Mongia *et al.* 2003). This approach relied heavily on measured data, which was not only expensive to acquire, but also might not be available during the design phase. As a consequence, the design curves, which were derived from the historical data, could only be extrapolated to a very limited design space. In order to meet increasingly stringent performance and emissions requirements, a comprehensive analysis capable of predicting combustor performance, emissions, and operatability is highly desirable. The need to lower design cost and reduce turn-around time also requires a more efficient analytical design tool. Recent progress in computer hardware, numerical algorithms, mesh generators, and physical modelling of turbulence, combustion and two-phase flows (Piomelli 1999; Colin *et al.* 2000; Lasheras & Hopfinger 2000;

† Author to whom correspondence should be addressed: vigor@psu.edu.

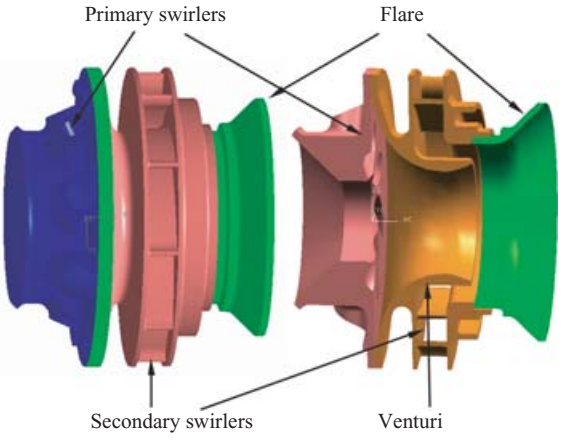

FIGURE 1. Schematic of a gas-turbine swirl injector assembly with radial entry.

Meneveau & Katz 2000; Moin 2002, 2004; Veynante & Vervisch 2002) have promoted computational combustor design methodologies to the main stage. In particular, large-eddy simulation (LES) techniques have begun to play a more important role in exploring turbulent flows in complex geometries for industrial applications under realistic operating conditions. Although much effort has been applied (Kim, Menon & Mongia 1999; Grinstein *et al.* 2002; Huang *et al.* 2003; Selle *et al.* 2004; Wang *et al.* 2004, 2005; Lu *et al.* 2005; James, Zhu & Anand 2006; Moin & Apte 2006), comprehensive model verification and validation against experimental data for operational injectors has not been conducted, except for the attempts by Selle *et al.* (2004) and Moin & Apte (2006) with limited benchmark. Furthermore, existing works provided only limited discussions of unsteady flow physics inside swirl injectors.

The present work is one of a series of studies (Mongia *et al.* 2001; Cai *et al.* 2003; Hsiao & Mongia 2003; Hsiao, Mongia & Vij 2003; Manampathy, Mongia & Jeng 2003; Stevens, Held & Mongia 2003) aimed at investigating detailed flow and combustion dynamics of gas-turbine injectors. The purpose is to establish and implement high-fidelity modelling techniques to explore the detailed flow evolution in full-scale injectors and combustors, and to extract the essential physics dictating the flow characteristics. As a specific example, we consider a swirl injector which has been used in several operational aircraft engines (figure 1). Such injectors are recognized for achieving high combustion efficiency. It also features an adequate margin for the lean blow-out (LBO) limit at low-power operations, and reduced NO_x and smoke emissions at high-power operations.

To characterize the injector flow field and to provide a benchmark database for numerical model validation, measurements were first made of non-reacting flows using the laser-Doppler velocimetry (LDV) technique (Mongia *et al.* 2001). A companion numerical analysis based on the Reynolds averaged Navier–Stokes (RANS) equations was then conducted to determine the flow field using a through-the-vane (TTV) modelling approach (Hsiao *et al.* 2003). The computational domain spanned from the upstream region of the swirler, i.e. the diffuser, where the boundary conditions were well posed for the analysis, to the downstream regime of the chamber. The flow fields within the swirlers were calculated as part of the solution. Grid-independent results were obtained and validated against the LDV data. The standard k–ε model provided reasonable agreement with experimental measurements. Several deficiencies, however,

were observed in the RANS simulation for the counter-rotating configuration. For example, at the injector exit, the RANS modelling approach resulted in a counter-clockwise inner azimuthal velocity profile driven by the swirling jets from the primary air passage, and a clockwise outer profile from the secondary swirl vanes. In contrast, the LDV data showed strong mixing between the primary and secondary air streams, and revealed only clockwise velocity profiles.

In the current study, a large-eddy-simulation technique is used to investigate the turbulent swirling flow in the gas-turbine swirl injector shown in figure. 1. Both co- and counter-rotating configurations are considered. Since the flow structure inside the injector cannot be acquired experimentally, the numerical analysis provides much useful information about the underlying mechanisms for turbulent mixing and energy transfer in strong swirling flows. The paper is organized as follows. Section 2 briefly describes the experimental set-up and flow conditions. Sections 3 and 4 present the theoretical formulation and numerical analysis, respectively. The results are discussed in § 5, followed by the conclusions in § 6.

2. Experimental set-up and flow conditions

Figure 1 shows the swirl injector considered herein, consisting of eight counter-clockwise (looking from the downstream side) elliptical primary jets, ten clockwise secondary vanes, a venturi and a flare. The air swirlers are designed to generate strong swirling flows for atomizing the liquid fuel issuing from the centrebody. The resultant droplets, carried by the primary air stream, mix with the countre-rotating secondary air to further promote rapid fuel–air mixing. When the engine operates at a high-power level, part of the liquid fuel injected from the centrebody impinges onto the surface of the venturi and forms a liquid film, which is then atomized to a spray of fine droplets by the strong counter-rotating shear flows near the edge of the secondary swirler.

Only single-phase non-reacting flows were treated in the present work as the first step in a systematic LES study of swirl injector flow and flame dynamics at operational device scales. The inlet air was supplied with a 4 % pressure differential across the injector at 1 atm and 291 K. The diameter, $D_0 = 27$ mm, and the mean axial velocity, $U_0 = 30\,\mathrm{m\,s^{-1}}$, at the downstream end of the secondary swirl vanes were employed as the reference length and velocity, respectively. The corresponding Reynolds number is 5.4×10^4.

Measurements were made of the velocity field downstream of the injector (figure 2). The injector was flush mounted on the dome plate of a square chamber with optical access. The chamber measured a width of 76.2 mm and a length of 356 mm, so that no reverse flow was observed at the exit. The coordinate system is so defined that the x-axis is aligned with the injector centreline. A two-component LDV system was employed to measure the three velocity components on the transverse planes along the length of the chamber. In the upstream region, in which rapid flow variations occurred, a total of 53 surveys were conducted at axial locations spaced 2 mm apart. The first sampling station was 3 mm downstream of the flare exit. In the downstream region, a total of 12 surveys were performed at axial locations with a wider spacing of 4 mm. For the first 16 axial locations (x = 32–62 mm), each velocity survey on the transverse plane was comprised of 73 measurement points to resolve the fine structure of the turbulent flow, whereas in the remaining region, a coarser resolution of 37 points was used to capture the overall flow development. The total number of measurements is 2981, covering a region of $152 \times 76.2 \times 76.2$ mm^3. A more detailed

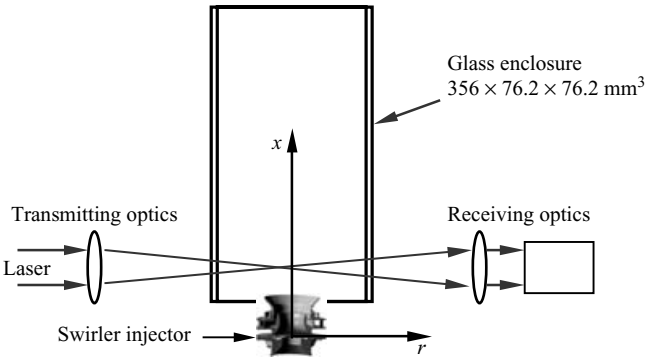

FIGURE 2. Experimental set-up for measuring the velocity field downstream of the injector using laser-Doppler velocimetry.

description of the experimental set-up and diagnostic equipment can be found in Cai *et al.* (2003).

3. Theoretical formulation

The present analysis is based on a large-eddy-simulation (LES) technique, in which large-scale turbulent structures are directly computed and small dissipative structures are modelled. Mathematically, the LES methodology begins with the filtering of small-scale effects from large-scale motions in the full conservation equations. The formulation treats the Favre-filtered conservation equations of mass, momentum and energy in three dimensions, written in the following conservative form:

$$\frac{\partial \bar{\rho}}{\partial t} + \frac{\partial \bar{\rho}\tilde{u}_j}{\partial x_j} = 0, \tag{1}$$

$$\frac{\partial \bar{\rho}\tilde{u}_i}{\partial t} + \frac{\partial(\bar{\rho}\tilde{u}_i\tilde{u}_j + \bar{p}\delta_{ij})}{\partial x_j} = \frac{\partial\left(\bar{\tau}_{ij} - \tau_{ij}^{sgs}\right)}{\partial x_j}, \tag{2}$$

$$\frac{\partial \bar{\rho}\tilde{e}_t}{\partial t} + \frac{\partial[(\bar{\rho}\tilde{e}_t + \bar{p})\tilde{u}_j]}{\partial x_j} = \frac{\partial\left(-\tilde{q}_i + \tilde{u}_j\tilde{\tau}_{ij} - Q_i^{sgs} + \sigma_i^{sgs} - H_i^{sgs}\right)}{\partial x_i}, \tag{3}$$

where an overbar denotes the spatial-filtering operation and a tilde the Favre-filtering operation, i.e. $\tilde{f} \equiv \overline{\rho f}/\bar{\rho}$. The variables ρ, u_i, p, e, q_i and τ_{ij} represent the density, velocity, pressure, specific total energy, heat flux and viscous stress, respectively. The equation of state for an ideal gas is used. The subgrid-scale SGS terms are

$$\tau_{ij}^{sgs} = \overline{\rho}(\widetilde{u_i u_j} - \tilde{u}_i\tilde{u}_j), \tag{4}$$

$$D_{ij}^{sgs} = (\overline{\tau}_{ij} - \tilde{\tau}_{ij}), \tag{5}$$

$$Q_i^{sgs} = (\overline{q}_i - \tilde{q}_i), \tag{6}$$

$$H_i^{sgs} = (\overline{\rho}(\widetilde{e_t u_i} - \tilde{e}_t\tilde{u}_i) + (\overline{pu}_i - \overline{p}\tilde{u}_i), \tag{7}$$

$$\sigma_i^{sgs} = (\overline{u_j\tau_{ij}} - \tilde{u}_j\tilde{\tau}_{ij}). \tag{8}$$

They are treated using the Smagorinsky model for compressible flows proposed by Erlebacher *et al.* (1992) because of its reasonable accuracy and simplicity in simulations of turbulent flows in complex geometries. The anisotropic part of the sgs stresses, (4), is treated using the Smagorinsky model, whereas the isotropic part, τ_{kk}^{SGS},

is modelled with a formulation proposed by Yoshizawa (1986),

$$\tau_{ij}^{SGS} - \tfrac{1}{3}\delta_{ij}\tau_{kk}^{SGS} = -2v_t\overline{\rho}(\tilde{S}_{ij} - \tfrac{1}{3}\delta_{ij}\tilde{S}_{kk}), \tag{9}$$

$$\tau_{kk}^{SGS} = 2\overline{\rho}k^{SGS} = 2C_I\overline{\rho}(D\Delta)^2|\tilde{S}|^2, \tag{10}$$

where

$$v_t = C_R(D\Delta)^2|\tilde{S}|, \quad \tilde{S}_{ij} = \tfrac{1}{2}\left(\frac{\partial\tilde{u_j}}{\partial x_i} + \frac{\partial\tilde{u_i}}{\partial x_j}\right), \quad k^{SGS} = \tfrac{1}{2}(\widetilde{u_i u_i} - \tilde{u_i}\tilde{u_i}).$$

The dimensionless quantities C_R and C_I are the compressible Smagorinsky model constants. Yoshizawa (1986) proposed an eddy-viscosity model for weakly compressible turbulent flows, using a multi-scale direct-interaction approximation method, and suggested $C_R = 0.012$ and $C_I = 0.0066$ based on theoretical arguments. The Van Driest damping function D is used to take into account inhomogeneities near the wall boundary (Piomelli, Moin & Ferziger 1988), and is expressed as

$$D(y^+) = 1 - \exp[-(y^+/25)^3], \tag{11}$$

where $y^+ = u_\tau y/v$, $u_\tau = \sqrt{\overline{\tau}_w/\overline{\rho}}$, and $\overline{\tau}_w$ denotes the wall stress.

The subgrid energy flux term, H_j^{SGS}, is modelled as

$$H_j^{SGS} = -\overline{\rho}\frac{v_t}{Pr_t}\frac{\partial\tilde{H}}{\partial x_j} = -\overline{\rho}\frac{v_t}{\mathrm{Pr}_t}\left(\frac{\partial\tilde{h}}{\partial x_j} + \tilde{u}_i\frac{\partial\tilde{u}_i}{\partial x_j} + \frac{\partial k^{SGS}}{\partial x_j}\right), \tag{12}$$

where $\tilde{H}$ represents the filtered specific total enthalpy. The turbulent Prandtl number, Pr_t, assumes a conventional value of 0.7 (Zang, Dahlburg & Dahlburg 1992). The SGS viscous diffusion term, σ_i^{SGS}, is neglected in the present study because of its small contribution in the energy equation (Martin, Piomelli & Candler 2000). The nonlinearity of the viscous stress term, D_i^{SGS}, and the heat flux term, Q_i^{SGS}, is invariably neglected (Piomelli 1999).

As will be shown later, the static Smagorinsky model outlined above leads to results in good agreement with measured mean velocities and turbulent properties over an extended spatial domain. A companion study employing a dynamical SGS model (Germano *et al.* 1991), which has been most successful for transitional and near-wall flows, does not exhibit any superior performance of such a model for the present configuration, in which the unbounded highly turbulent shear flows play a dominant role in determining the overall flow evolution within the injector. The maximum difference of the calculated mean axial velocities based on the static and dynamic SGS models is $2.1\,\mathrm{m\,s^{-1}}$, i.e. $0.07\,U_0$. The average difference of the mean axial velocity is 1.9 % over the entire field, which is in the range of experimental uncertainties.

Owing to the limitations of computing resources and the numerical algorithm, it is difficult to explore the flow dynamics in a domain consisting of the entire injector (including the flow passage within the swirler) and the air delivery system (i.e. diffuser) upstream of the injector using computational fluid dynamics (CFD) codes based on structure grids. Even for unstructured grids, the numerical resolution and accuracy within the context of LES may raise concerns. The computational domain thus spans from the exits of the primary jets and secondary swirler. To reduce the uncertainties arising from the inlet boundary conditions, the mean-flow velocities and total temperature at the computational inlet were obtained by extracting the results from a RANS-based simulation (Hsiao *et al.* 2003), for which a through-the-vane approach was employed to determine the flow field extending from the diffuser, through the swirlers, to the exit of the chamber. The pressure was determined using

a simplified one-dimensional momentum equation in the direction normal to the inlet boundary. Turbulence was provided by superimposing broadband noise with a Gaussian distribution on the mean velocity profile with its intensity extracted from the RANS simulation. A parametric study based on the RANS approach was conducted by varying the inlet turbulence intensity by $\pm 25\,\%$ for the present computational domain. Calculated flow fields were found to be insensitive to the incoming turbulence intensity because of the strong shear flows generated within the swirl injector.

The outlet boundary conditions must be properly specified. A comprehensive analysis of the effects of outlet boundary conditions was conducted by Hsiao & Mongia (2003) using a RANS approach. The efforts included the variation of the chamber length and inclusion of an additional exhaust zone. Results indicated that a computational domain covering a chamber length of $11D_0$ is sufficiently large to minimize the influence of outflow boundary conditions on the injector flow evolution. At the exit, the back pressure was specified according to a simplified radial momentum equation,

$$\frac{\partial p}{\partial r} = \frac{\rho U_\theta^2}{r}, \tag{13}$$

where U_θ denotes the time-mean azimuthal velocity. Because the experiment was conducted at ambient conditions, the pressure on the wall of the chamber exit was fixed at 1 atm. The other four flow variables (i.e. three velocity components and temperature) were determined by assuming zero gradients. Finally, the no-slip adiabatic conditions were applied to all solid walls.

4. Numerical approach

The flow field in the present study falls in the low-Mach-number regime, in which the large disparity between the acoustic and flow speeds substantially degrades the efficiency of conventional density-based algorithms. A preconditioning technique augmented by a dual-time integration procedure was employed to circumvent this difficulty (Hsieh & Yang 1997). The governing equations were discretized using an explicit four-step Runge–Kutta method to evaluate the pseudo-time derivatives with a Courant–Freidricks–Levy (CFL) number of 1.1. A generalized second-order backward differencing scheme was used to evaluate the physical time derivatives. The physical time-marching step is 5×10^{-3} ms, i.e. $\Delta t = 5.6 \times 10^{-3} D_0/U_0$. Implementation of the dual time-stepping technique allowed for flexibility in selecting the integration step in the physical time domain. The approach was benchmarked against a commonly used four-step Runge–Kutta scheme (RK4) for the evolution of isotropic turbulence in a uniform mean flow. The result indicates that the numerical dissipation of the present density-based code in simulations of turbulent flows at low Mach numbers is insensitive to the specific time-marching scheme selected if a modest CFL number is used (Wang *et al.* 2005). This may be attributed to the maximum allowable time step for a density-based scheme being much smaller than the turnover time of a grid-sized eddy.

Spatial discretization was achieved using a second-order accurate centre-differencing methodology, along with the employment of a fourth-order artificial dissipation in order to prevent numerical oscillations at high wavenumbers. To minimize numerical contaminations, the coefficient of the dissipation term was carefully selected to be $\varepsilon_4 = 0.01$. The spatial accuracy and related numerical dissipation were assessed by

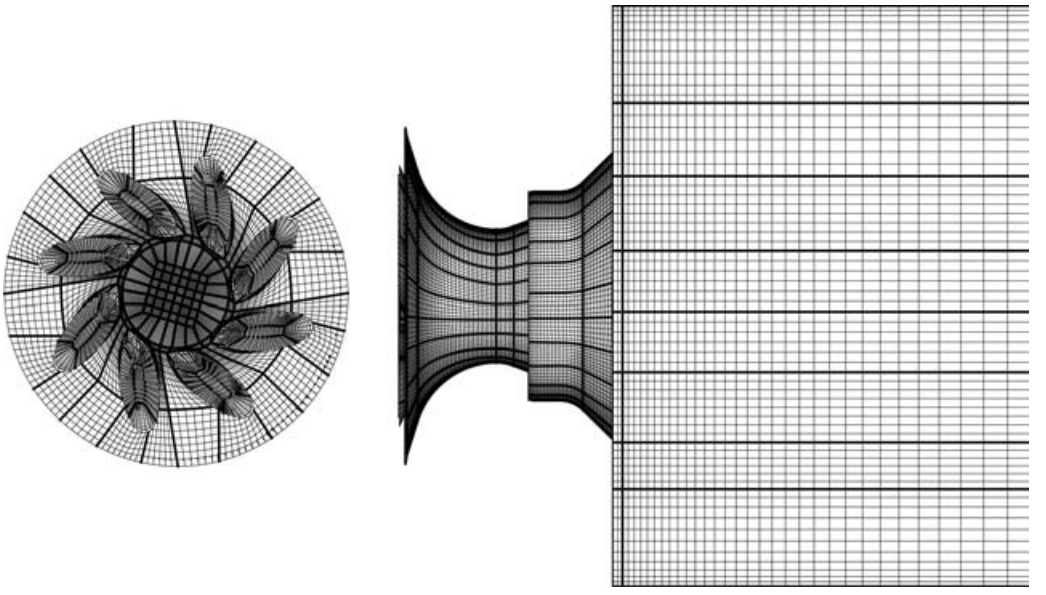

FIGURE 3. Grid system and domain decomposition. Thin lines: mesh; thick lines: partition boundary; counter-rotating case.

considering a benchmark problem of decaying isotropic turbulence. Calculations using both second and fourth-order spatially accurate schemes combined, respectively, with fourth- and sixth-order dissipation were performed on a $32 \times 32 \times 32$ grid for an isotropic turbulent flow in a cubic box of a width 2π with periodic boundary conditions. Excellent agreement was obtained with the experimental measurement (Comte-Bellot & Corrsin 1971) and DNS (direct numerical simulation) calculation in terms of the decay rate of the turbulent kinetic energy (TKE). The effects of SGS and numerical dissipation were further examined by either turning on/off those terms or reducing their values by half in the present simulations of injector flows. When the SGS terms were turned off, unphysical oscillations took place in the flow field. A concurrent decrease in numerical dissipation resulted in an overflow of the calculation. When the SGS terms were activated, the solution became stable even if ε_4 was reduced by half. The numerical method and grid resolution employed in the present study appeared to be relevant and did not give rise to a dissipative solution.

The complex geometry of the injector poses a serious challenge in generating the numerical grid. The injector configuration was first created with computer-aided-design (CAD) software, and then treated using a block-based structured hexahedral grid system. A total of 1620 blocks were employed for domain decomposition in order to resolve the geometric complexity of the hardware (figure 3). The overall grid system includes two million internal cells; its quality was carefully examined to ensure that no skew cell exists to hinder numerical convergence. The mean cell size inside the injector is 0.35 mm, which is sufficient to resolve the turbulence length scales in the inertial sub-range of the turbulent energy spectrum, as will be discussed later. The 1620 blocks were loaded on 48 CPUs for parallel processing. Since each processor treated more than one block, a weight function was used to obtain an appropriate load balance to achieve high computational efficiency. This is an important feature for a numerical solver dealing with block-based structured grids in a distributed computing environment.

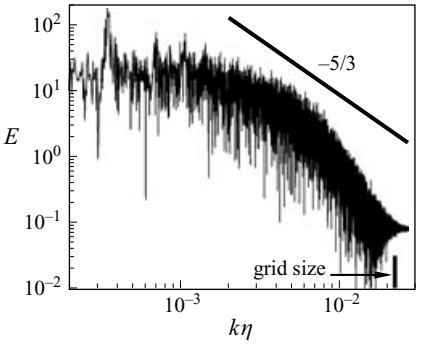

FIGURE 4. Spectrum of turbulent kinetic energy at $x/D_0 = 0.47$, $y/D_0 = -0.17$ and $z/D_0 = -0.07$. Counter-rotating case.

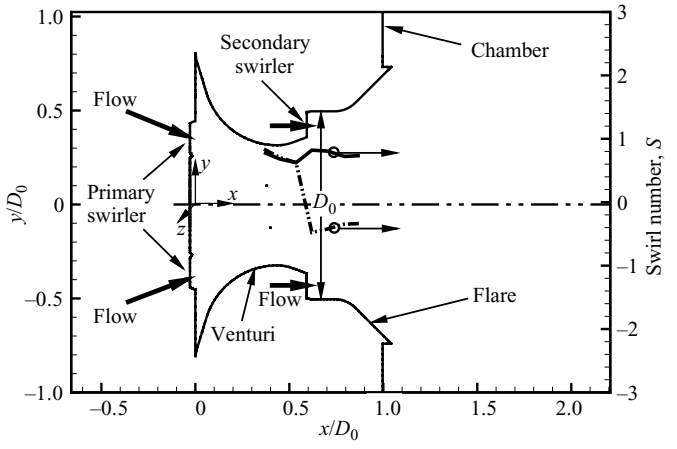

FIGURE 5. Injector schematic and distributions of swirl numbers of two different flow configurations. Solid line: counter-rotating; dashed line: co-rotating.

A multi-block technique based on a domain decomposition method was implemented to facilitate parallel processing, along with the use of the message passing interface (MPI) for exchanging information among processors. Each calculation was performed over an extended time period to ensure the establishment of a stationary flow field. Data was then collected for 110 ms ($122\,D_0/U_0$) to obtain statistically meaningful turbulence properties.

Figure 4 shows the spectrum of the turbulent kinetic energy at the location of $x/D_0 = 0.47$, $y/D_0 = -0.17$, and $z/D_0 = -0.07$ for the counter-rotating case. The origin of the coordinates is defined at the centre of the injector entrance plane (figure 5). The wavenumber is denoted by k. The Kolmogorov scale ($\eta \sim D_0\,Re^{-3/4}$) is estimated to be 8 μm and the Taylor scale ($l_T \sim D_0\,Re^{-1/2}$) 120 μm, according to the Reynolds number of 5.3×10^4. Here, Taylor's hypothesis is applied to approximate spatial correlations using temporal correlations, since the original data is the velocity–time traces at single points, from which spatial correlations cannot be directly derived. An accurate conversion based on this hypothesis is limited to homogeneous turbulence with small turbulence intensity (Pope 2000). Although the present injector flow does not strictly satisfy this constraint, it can still be regarded as a good reference for data analysis. The large scales on the order of the characteristic length of the injector,

D_0, are around $\eta/D_0 \sim 3 \times 10^{-4}$, and most of the turbulent kinetic energy is carried by flow motions with normalized wavenumbers less than 2×10^{-3} (figure 4). The calculated turbulent kinetic energy follows the Kolmogorov–Obukhov ($-5/3$) law in the high wavenumber regime. The difference in turbulent kinetic energy between the peak of large-scale motions and resolved grid scales is three orders of magnitude. The average grid size is around 350 μm within the injector. The corresponding Taylor scale ($\sim$120 μm) is located in the inertial sub-range of the turbulent kinetic energy spectrum.

It is worth noting that the fraction of resolved turbulent kinetic energy (not shown), defined as the ratio of the resolved to the total TKE (i.e. the sum of resolved and sub-grid TKE), exceeds 95 % in the bulk of the flow field except in small regions near the inlet, in which the sub-grid TKE depends strongly on the inlet flow condition. Most energy-carrying large scales are well resolved. The result further corroborates the adequacy of the SGS model, numerical scheme, and grid distribution employed in the present approach.

5. Results and discussion

Both co- and counter-rotating configurations were investigated in the present study. The difference between the two cases lies in the orientation of the secondary swirl vanes, i.e. $U_{\theta,co} = -U_{\theta,counter}$ at the entrance. Figure 5 shows the variations of the swirl number, S, along the length of the injector. The swirl number is defined as the ratio of the axial flux of angular momentum to the product of the axial flux of axial momentum and the injector radius,

$$S(x) = \frac{\int \rho U_\theta U_x r \, \mathrm{d}A}{R(x) \int \rho U_x^2 \, \mathrm{d}A}. \tag{14}$$

Here, U_x and U_θ represent the axial and tangential components of the mean velocity, respectively, and $R(x)$ the radius of the injector interior. The bulk-flow rotating directions inside the chamber are different for the two cases, and the swirl number is considerably higher in the co-rotating case. In this study, more emphasis is placed on the counter-rotating case because of the availability of experimental data for post validation. The configuration with co-rotation is treated for comparison.

Figure 6 shows snapshots of the vorticity magnitude fields on a single longitudinal (x, r)- and three latitudinal (r, θ)-planes for the counter-rotating case. A central recirculating flow is seen downstream of the venturi, serving as a source of low-frequency flow evolution. Because of the strong shear between the through and recirculating flows, a vorticity layer is produced along the boundary of the recirculation zone, which subsequently rolls, tilts, stretches and breaks up into small vorticity bulbs. Another notable phenomenon is the high-frequency vortex shedding arising from the Kelvin–Helmholtz instabilities in both the axial and azimuthal directions, originating from the trailing edge of the venturi. A similar flow pattern was also observed by Wang *et al.* (2005) in a swirl injector with radial entry. The ensuing influence on the fuel/air mixing may be significant because the shear layer interacts with the thin fuel film on the surface of the venturi. The flow pattern on the r–θ (A–A) cross-section clearly illustrates the structures associated with the eight primary swirling jets. Such a complicated flow structure diminishes in the downstream region. The flow becomes predominantly axisymmetric after it passes the venturi (see cross-sections B–B and C–C in figure 6) owing to strong turbulent motion, indicating that the injector has good mixing characteristics.

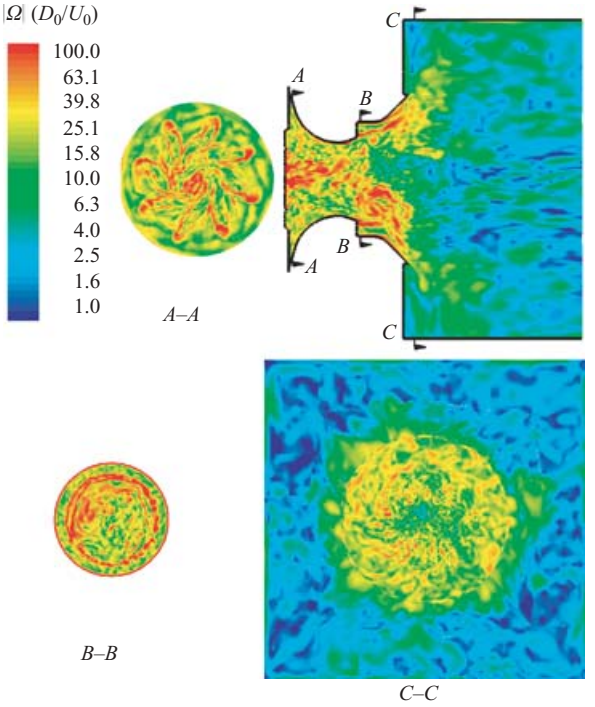

FIGURE 6. Snapshots of normalized vorticity-magnitude fields on x–r and r–θ cross-sections; counter-rotating case.

Figure 7 shows the three-dimensional streamlines in the time-mean flow field of the counter-rotation case. The iso-surfaces of zero axial velocity clearly indicate the existence of the central and corner recirculation zones. Two kinds of streamline are observed for the flow injected from the primary swirler with different radial locations. First, the flow injected far from the centreline rotates counterclockwise into the injector, then reverses its rotating direction after merging with the clockwise swirling flow injected through the secondary swirler, and finally flows clockwise into the chamber exit. Secondly, the flow injected near the centreline aligns with the axial axis and rotates at a high speed along the boundary of the central recirculation zone. The entire flow field exhibits a complex structure.

5.1. *Mean flow properties*

The mean-flow properties were calculated and compared with experimental data (Mongia *et al.* 2001). Figures 8 and 9 present the radial distributions of the time-mean velocity components and turbulence intensities in the axial, radial and azimuthal directions, respectively, at various axial locations. The scale in the zoom-in region ($x/D_0 > 4.27$) is increased three-fold to provide better resolution. Good agreement was achieved between the calculated and measured results except for the small discrepancies in the radial and azimuthal velocities immediately downstream of the injector exit. The flow split and velocity profiles specified at the inlet are indeed correct. A high-speed region with strong turbulence is observed near the trailing edge of the flare because of the rapid flow expansion resulting from the swirl motion and the existence of the central recirculating zone. The flow then becomes uniform as it travels downstream. The local maxima of all the velocity components at a given axial

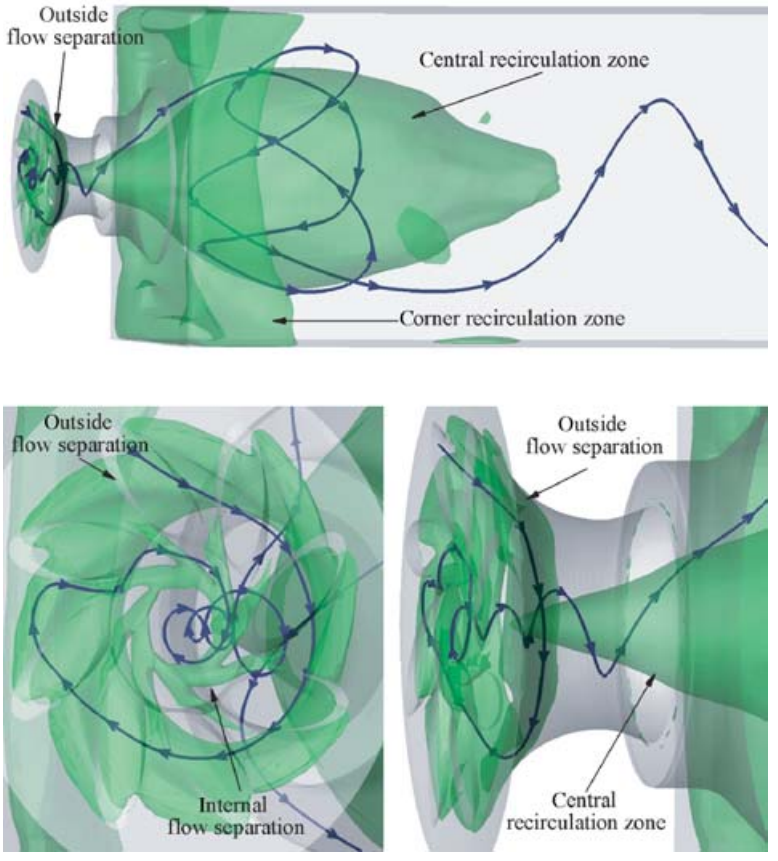

FIGURE 7. Streamline in mean flow field; counter-rotating case. The iso-surface denotes $U_x = 0$.

location decrease and move outward in the downstream region. The same trend is observed for the turbulence intensity, which tends to be more isotropic as the flow develops owing to the diffusion and dissipation effects. Similar phenomena were also reported in different types of swirl injector by Wang *et al.* (2004) and Lu *et al.* (2005).

Figure 10 shows the mean axial velocity field in the entire injector/chamber assembly. A large central toroidal recirculation zone (CTRZ), delineated by $U_x = 0$, is clearly observed. As a consequence of the strong swirling flow delivered into the injector through the primary swirler, steep pressure gradients are established in the radial direction to balance the centrifugal force and induce a low-pressure core around the centreline. The pressure is then recovered from the flow expansion and velocity decay in the downstream region. A positive (adverse) pressure gradient is formed along the centreline and finally causes flow reversal, a phenomenon commonly referred to as vortex breakdown. The recirculation zone originates from the middle of the venturi at $x = 0.15D_0$ and extends into the chamber at $x = 4.89D_0$. The result closely matches the experimental measurements, demonstrating that the present LES analysis predicts complex flow fields better than the RANS simulation (Hsiao *et al.* 2003), which over-predicted the length of the recirculation zone because of the lack of proper resolution of various length scales and inhomogeneities in the flow field.

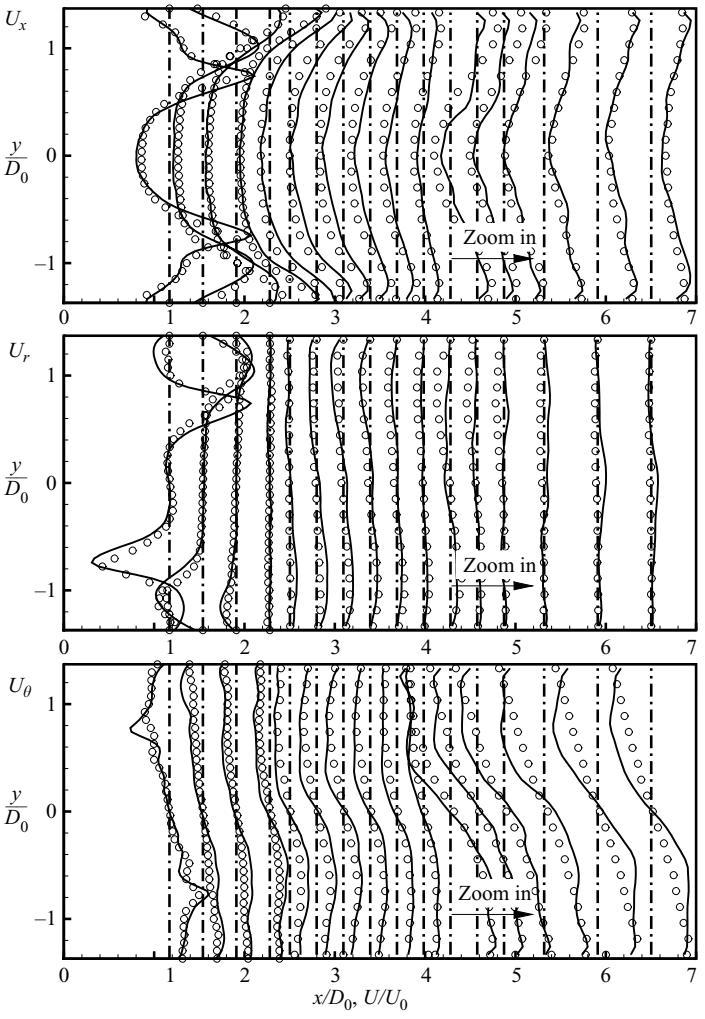

FIGURE 8. Radial distributions of normalized mean velocity components in axial, radial and azimuthal directions at various axial locations; counter-rotating case. The scale in the zoom-in region ($x/D_0 > 4.27$) is increased three-fold to provide better resolution. Line: simulation; symbol: experiment.

The central recirculating flow affects the injector performance in two areas. First, the reversed flow provides a low-speed region with high turbulence intensity, which promotes fuel/air mixing and stabilizes combustion over a broad range of operating conditions. This feature is one of the primary reasons for implementing swirling flows in combustion devices for propulsion and power-generation applications. Secondly, the blockage induced by the recirculation zone reduces the effective flow passage area, and consequently increases the flow velocity in the outer region. The resultant strong shear stress near the wall, especially in the vicinity of the venturi surface, enhances the atomization of the injected fuel. It is worth noting that in an operational pre-filming air-blast injector under fully loaded conditions, part of the liquid fuel injected from the fuel nozzle impinges onto the venturi surface and forms a thin film, which must be atomized to a spray of fine droplets by local shear flows. The flow field near the

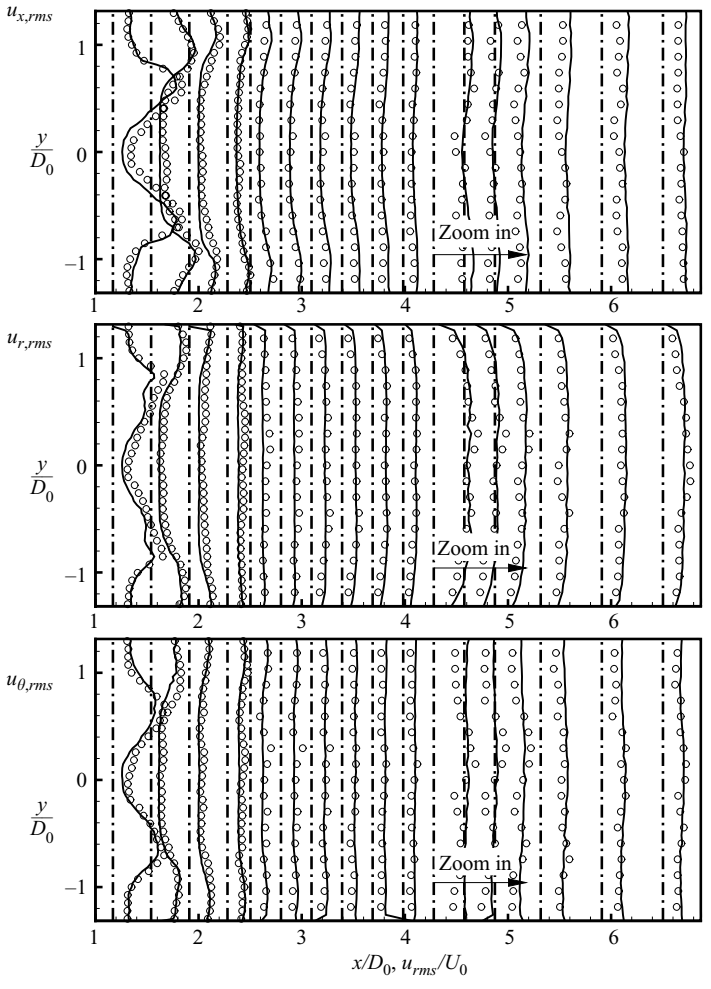

FIGURE 9. Radial distributions of normalized turbulence intensities in axial, radial and azimuthal directions at various axial locations; counter-rotating case. The scale in the zoom-in region ($x/D_0 > 4.27$) is increased three-fold to provide better resolution. Line: simulation; symbol: experiment.

injector wall plays a crucial role in dictating the liquid sheet breakup and droplet formation processes.

Figure 11 shows the time-mean angular momentum ($\Omega = \rho r u_\theta$) field, where solid and dashed lines denote positive and negative values, respectively. Part of the counter-clockwise (positive) swirling flows injected through the primary swirler first converge to the centreline, and then travel downstream outside the central recirculation zone. High azimuthal velocity is induced near the centreline during the flow-converging process because of the conservation of angular momentum. A minimum pressure core is consequently generated and the flow soon reverses behind this region. The reversed flow promotes the diverging-flow pattern. When the counter-clockwise swirling flows merge with the stronger clockwise swirling flows injected through the secondary swirler, the latter dominates the rotation direction of the bulk flow. Thus, the flow exiting the injector rotates clockwise.

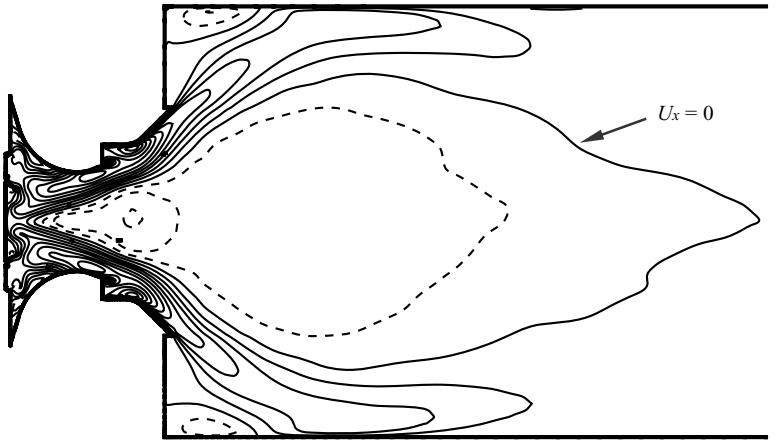

FIGURE 10. Contours of normalized long-time averaged axial velocity. Range from –0.6 to 2.2 with increment of 0.2. Solid line: positive values; dashed line: negative values; counter-rotating case.

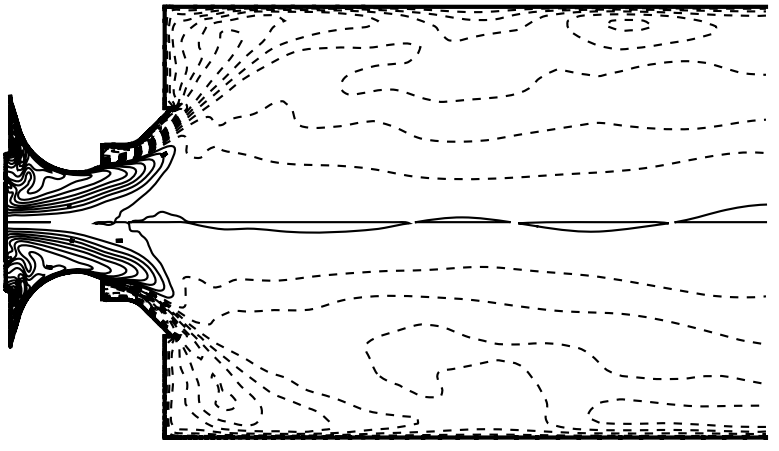

FIGURE 11. Contours of normalized long-time averaged angular momentum. Range from −0.9 to 0.6 with increment of 0.05. Solid line: positive values; dashed line: negative values; counter-rotating case.

In addition to the central recirculation zone, a corner recirculation zone (CRZ) exists downstream of the flare. Owing to the rapid flow expansion resulting from the strong swirling motion and geometric configuration, the corner recirculation zone is much shorter than the central recirculation zone. The azimuthal velocity component prevails in the corner recirculation zone, with the other two components being relatively weaker, owing to the geometric constraints. The conservation of angular momentum, along with strong turbulent motion and fewer circumferential geometric constrains, renders the distribution of the azimuthal velocity relatively uniform – a profile that is less sensitive to flow reversal. A similar phenomenon was observed in the central recirculation zone.

The turbulent kinetic energy field shown in figure 12 exhibits three different high-intensity regions inside the injector. Region 1, formed by the merging of the eight swirling jets, includes the head-end region near the centreline, where the liquid

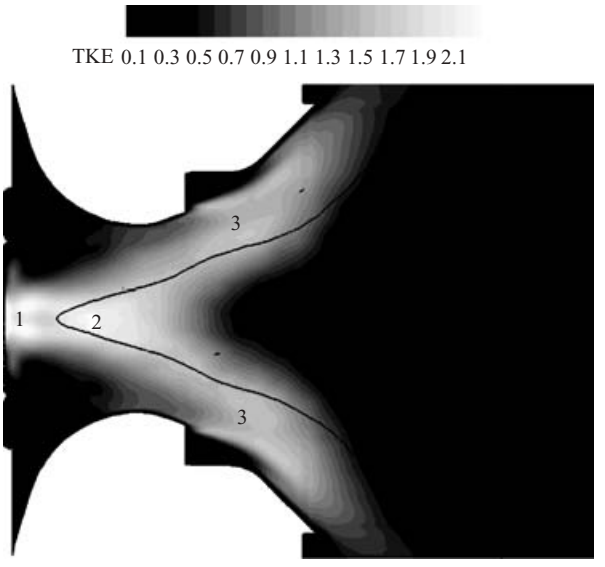

FIGURE 12. Normalized turbulent kinetic energy field; counter-rotating case.

fuel is discharged. The vigorous flow motion promotes primary liquid breakup and atomization. Region 2 covers the stagnation point of the central recirculating flow. A precessing vortex core (PVC) is observed originating from this region, and will be addressed in detail in the following section. Both the vortex precession and flow recirculation enhance local flow oscillations at the stagnation point. Region 3 consists of the field surrounding the central recirculation zone in the main flow passage. Strong shear layers develop, especially when the primary swirling flow merges with the counter-rotating flow through the secondary swirler. The intense motion in the radial direction accelerates the development of the Kelvin–Helmholtz instability in the liquid film issuing from the trailing edge of the venturi. The strong shear force associated with the counter-rotating flows in the azimuthal direction also enhances the atomization process. Thus, the flow structure in the present injector provides an effective capability to atomize the liquid film.

5.2. *Unsteady flow evolution: vortex precession*

Although the mean flow field is axisymmetric because of the geometric symmetry of the injector configuration, the instantaneous flow field is highly dynamic. In particular, the central recirculating flow precesses around the centreline at a well-defined frequency. Such a precessing vortex core is often present when vortex breakdown occurs in a high-Reynolds-number flow, such as turbulent swirling flows in cyclone chambers and combustion devices (Gupta, Lilley & Syred 1984; Lucca-Negro & O'Doherty 2001; Syred 2006). Figure 13 shows a snapshot of the PVC structure delineated by an isobaric surface of $p = 97$ kPa. The low-pressure core aligns with the centreline in the head-end region, and then issues from the centreline at the stagnation point of the central recirculating flow in a spiral form. The PVC structure twists against the direction of the flow rotation, although the whole coherent structure follows the same direction. The frequency of this precessing process, f, is 1266 Hz, and the corresponding Strouhal number, $S_t = fD_0/U_0$, is 1.1. Figure 14 shows the temporal evolution of the pressure field and streamlines on a longitudinal plane ($z = 0$). The thick line represents the contour of zero mean axial velocity, $U_x = 0$.

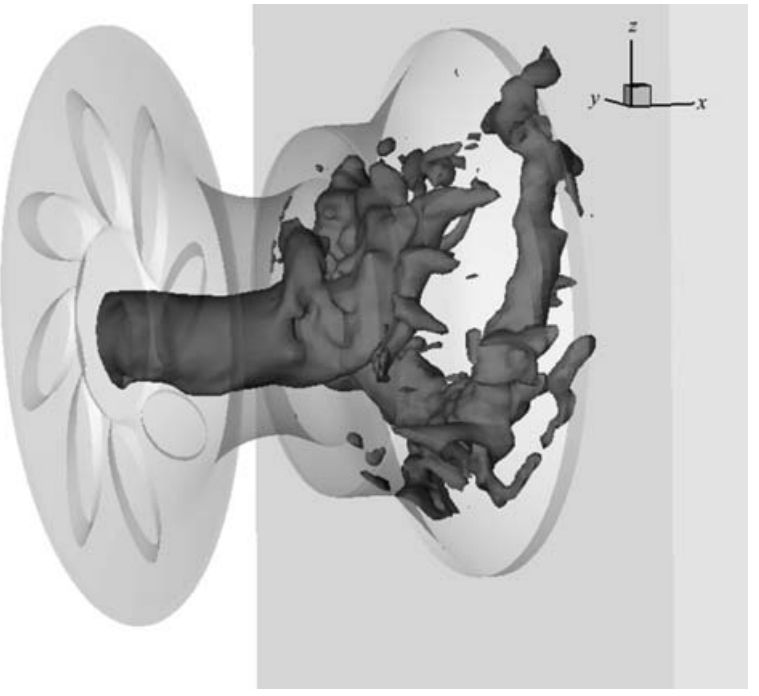

FIGURE 13. Snapshot of isobaric surface of $p = 97\,\text{kPa}$, showing the existence of a precessing vortex core; counter-rotating case.

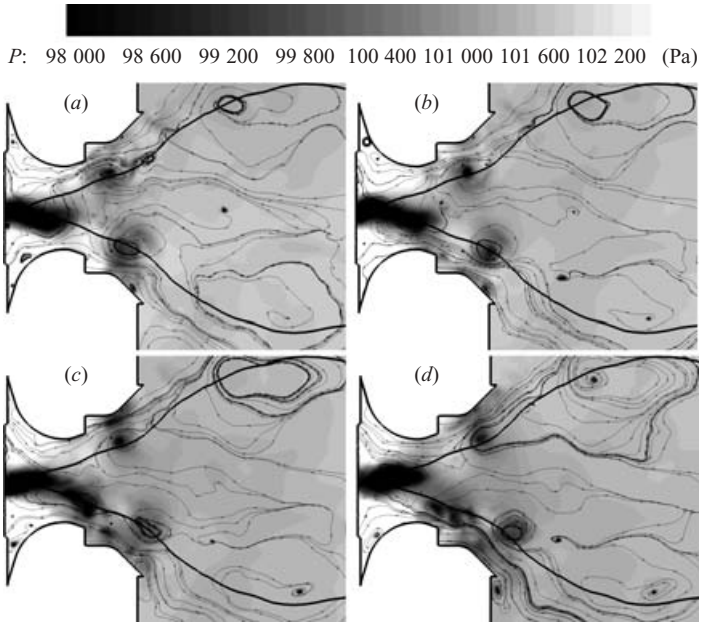

FIGURE 14. Temporal evolution of pressure field and streamlines with a time increment of 0.1 ms; thick line: contour of $U_x = 0$. Counter-rotating case.

The vortex core is visualized by clustered streamlines around the low-pressure core, which derive from the centreline in the downstream region and are pushed away outward. Furthermore, the vortex core is located outside of the region defined by zero axial velocity. The situation is consistent with the experimental observation of Syred & Beer (1972), in which the PVC was located between the zero axial-velocity and dividing surfaces in the outer region of the recirculation zone. When the coherent structures rotate in the injector, the large vortices are peeled off from the spiral core periodically and are convected downstream by the local flow.

Novak & Sarpkaya (2000) found that the direction of the spiral winding changed randomly in their experimental study of turbulent swirling flows at high Reynolds numbers. Lucca-Negro & O'Doherty (2001) reviewed the twist direction for the spiral-form of vortex breakdown, but drew no definite conclusions. Although vortex precession at low Reynolds numbers is not identical to the spiral-form vortex breakdown, the precessing process can be considered as periodic spiral motion in the conical-form turbulent vortex breakdown observed by Novak & Sarpkaya (2000). To our knowledge, no definite conclusion has been reached so far on the twist direction of the PVC. Figure 15 reveals the mechanism dictating the twist direction in the present study. The yellow surface is the iso-surface of the angular velocity of $\omega = 2400\pi\,\mathrm{s}^{-1}$ of the mean flow field. The corresponding frequency is about 1200 Hz, i.e. $S_t = 1.1$, which is close to the frequency of vortex precession. Because the flow is introduced as eight converging swirling jets, the angular velocity increases and reaches its local maximum near the centreline. The swirling flow outside this iso-surface lags the precessing vortex core, denoted by the isobaric surface of 95 kPa shown in green. On the other hand, the flow inside the iso-surface of $S_t = 1.1$ rotates faster than the vortex core. As a result, the inner flow drives the vortex core azimuthally, whereas the outer flow exerts an opposite influence. Such a spatial variation of the angular velocity in the flow field produces a counter-twist spiral coherent structure in the injector. The PVC structure resembles that observed by Selle *et al.* (2004), who simulated non-reacting and reacting flows in an industrial gas turbine burner. Similar phenomena were also observed by Wang *et al.* (2004, 2005) and Lu *et al.* (2005). In swirling flows with a convergent structure, such as those in radial-entry swirl injectors, the counter-twist PVC appears to be prevalent over the co-twist one.

It is well established that the origin of vortex breakdown and precession in a swirl injector is sensitive to the flow condition in the upstream region. In addition, the vortex core may swing along the axis of the swirling flow, rendering a strong coupling between the flow fields within and upstream of the injector. Care must be exercised in analysing calculated results to ensure the simulation accuracy. This is especially necessary in the current study, given that the upstream region was not treated within the context of LES, and that no experimental data were available for specifying the instantaneous flow evolution at the injector inlet. In the present configuration, the PVC induced by the incoming swirling flow resides within the injector. It does not move upstream through the primary jet flow passage, owing to the convergence of the swirling flow at the origin of the PVC. The secondary swirler and divergent flare also help confine the vortex breakdown. Thus, the geometric constraints of the injector prohibit the PVC from swinging freely along the axial axis. To further explore this phenomenon, a companion LES study was conducted by including the entire flowpath from the diffuser, through the swirlers, to the downstream region of the injector by means of a pressure-based implicit solver with second-order accuracy in both time and space. The calculated velocity spectra indicate that the vortex precession influences only the local flow field surrounding the core. Any disturbances arising from the PVC

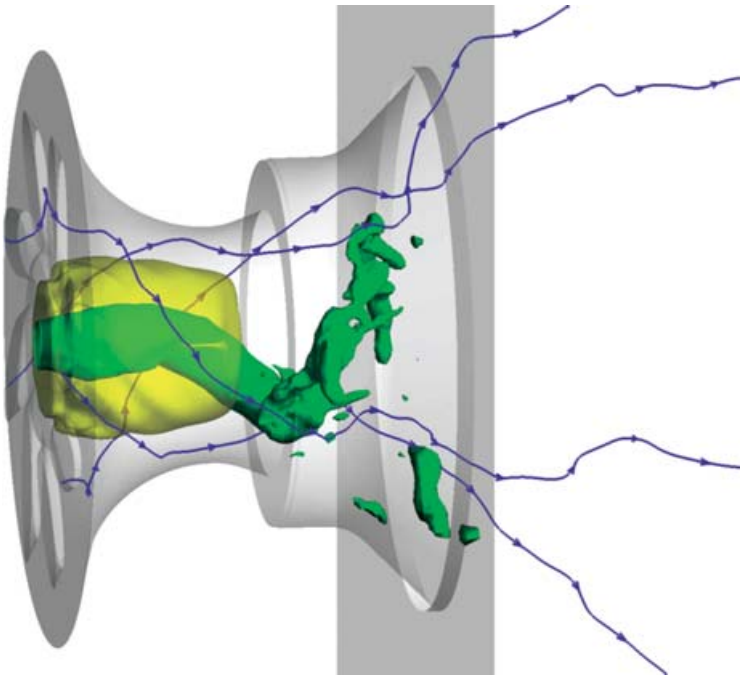

FIGURE 15. Instantaneous isobaric surface of $p = 95\ kPa$ (green) and iso-surface of angular velocity of $\omega = 2400\pi\ s^{-1}$, i.e., 1200 Hz (yellow), based on time-mean flow field; counter-rotating case.

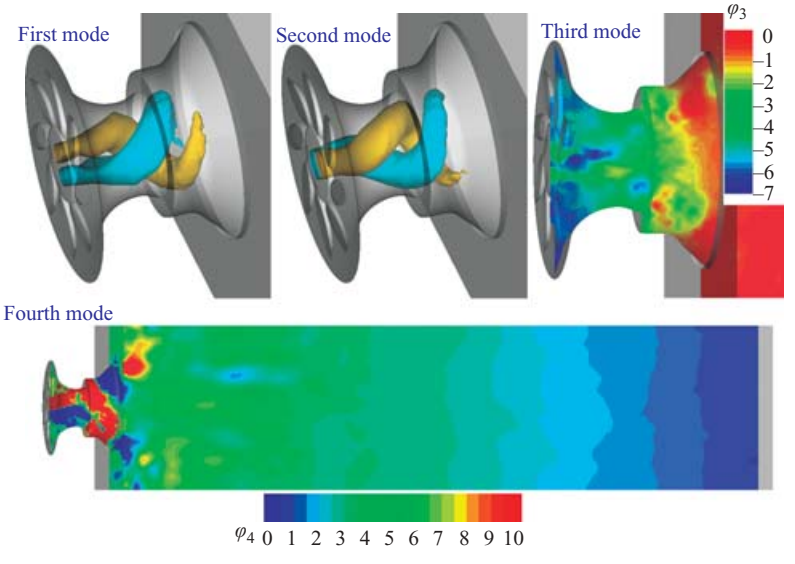

FIGURE 17. First four POD modes of normalized fluctuating pressure field; counter-rotating case.

are soon damped as they travel outward. Such a lack of interactions with the flow motions in the upstream region of the injector provides another justification for the current approach.

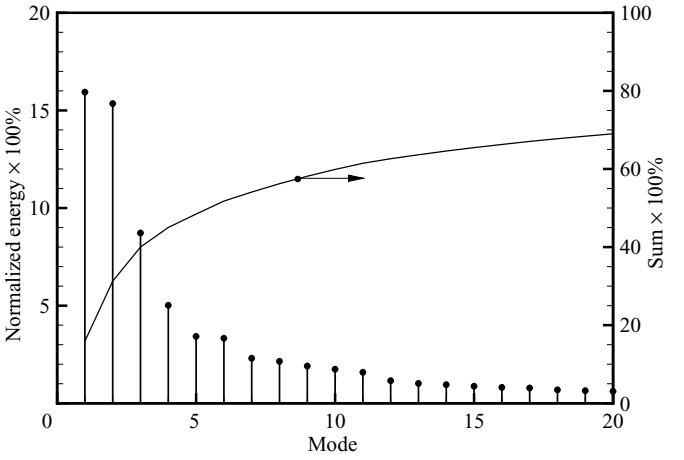

FIGURE 16. Energy distribution of POD modes based on pressure field; counter-rotating case.

5.3. *Flow dynamics analysis*

A proper-orthogonal-decomposition (POD) analysis was employed in the present study to extract the most energetic coherent structures from the calculated data. Analysis of this kind has been used in our previous work (Lu *et al.* 2005; Wang *et al.* 2005; Huang, Wang & Yang 2006) to identify the dominant mechanisms dictating the flow development. For a given pressure field, $p(\boldsymbol{x}, t)$, the POD analysis can determine a set of orthogonal functions $\varphi_j(\boldsymbol{x})$, $j = 1, 2, \ldots$, so that the projection of p onto the first n functions

$$\hat{p}(\boldsymbol{x}, t) = \overline{p}(\boldsymbol{x}) + \sum_{j=1}^{n} a_j(t)\varphi_j(\boldsymbol{x}) \tag{15}$$

has the smallest error, defined as $E(\| p - \hat{p} \|^2)$. Here, $a_j(t)$ represents the temporal variation of the jth mode. A more complete discussion of this subject can be found in Berkooz, Holmes & Lumley (1993).

The analysis was conducted using 200 snapshots of the three-dimensional pressure fields with an increment of $0.12D_0/U_0$ (0.11 ms), corresponding to a cutoff Strouhal number of 4 ($f = 4.5$ kHz). Figure 16 shows the energy distribution of the first ten POD modes. The associated mode shapes are shown in figure 17. Here the energy of the jth mode, E_j, is defined as

$$E_j \equiv E(\|a_j(t)\varphi(x)\|^2). \tag{16}$$

The energy carried by the first two modes, whose dominant frequencies are identical, exceeds 30 % of the total energy of the fluctuating pressure field. The mode shapes and time-varying coefficients further indicate that they are two complementary modes of a spirally rotating motion, i.e. vortex precession, with a harmonic at $S_t = 1.1$ ($f = 1266$ Hz). Such a motion is the dominant mechanism in the cold flow evolution.

The shape of the third mode clearly reveals a standing acoustic wave inside the swirl injector, with a dominant frequency of $S_t = 2.2$ (2450 Hz). Because of the large cross-sectional area of the chamber, the injector exit can be considered to be acoustically open. The small fraction of the open area at the injector entrance plane leads to an acoustically closed boundary. Consequently, the characteristic frequency of the

longitudinal standing wave inside the injector is around 2500 Hz ($S_t = 2.3$, matching closely the frequency of the third POD mode. The fourth mode has a dominant frequency of $S_t = 0.2$ (210 Hz), which corresponds to the standing acoustic wave in the chamber and is confirmed by the mode shape shown in figure 17 and a companion acoustic analysis. This mode is dependent on the geometry and exit boundary condition of the chamber. Hence, it should not be treated as an intrinsic property of the injector flow. The seventh, eighth and ninth modes represents the higher harmonics of the vortex precession, a phenomenon that can also be validated by their respective mode shapes (not presented). The fifth and sixth modes arise from the flow evolution unrelated to the PVC.

The high-frequency motion at $S_t = 18$ (20 kHz), resulting from the Kelvin–Helmholtz instability downstream of the venturi, was not observed in the present POD analysis because its frequency greatly exceeds the POD cutoff frequency. Another POD analysis performed on a data set with a higher sampling frequency of $S_t = 45$ ($f = 50$ kHz) did not identify this motion either. The phenomenon may be attributed to the high-frequency motion downstream of the secondary swirler being a local phenomenon, which is not captured by the POD analysis conducted on the global flow field. Another reason is the occurrence of the azimuthal instability, which may overshadow the instability in the streamwise direction. Consequently, the coherent structures resulting from the shear-layer instability are not clear. A similar phenomenon was observed in the high swirl-number case in Wang *et al.* (2005), in which the Kelvin–Helmholtz instability in the axial direction was not the dominant flow mechanism at a high swirl number, although it played an essential role at a low swirl number.

In summary, the POD analysis clearly reveals two different flow patterns dictating the injector dynamics: precessing vortex motion and standing acoustic waves. The former determines the major flow evolution in the present swirl injector.

5.4. *Co-rotating swirling flow*

The influence of the inlet flow direction on the injector dynamics is explored by reversing the orientation of the secondary swirl vanes in such a manner that both the primary and secondary swirlers generate counterclockwise swirling flows. Figures 18 and 19 show the radial distributions of three velocity components and associated turbulence intensities in the chamber, respectively. The mean velocity field in the co-rotating case bears a close resemblance to its counterpart in the counter-rotating case, except that the former possesses a much longer central recirculation zone, owing to the stronger swirling motion. It is worth noting that the large recirculation zone reduces the effective flow passage in the injector, and consequently weakens the effects of the secondary swirling flow on the flow development within the venturi. Consequently, the injector flow evolution is mainly driven by the flow through the primary swirler. Only a modest difference is observed in the streamwise direction between the co- and counter-rotating cases. In the flare and chamber, the flow disparity is limited, except for a noticeable difference in the azimuthal velocity field and a lower axial velocity along the centreline in the co-rotating case, because of its higher azimuthal velocity.

In addition to the recirculation zone, another major difference between the two configurations lies in the distribution of turbulent kinetic energy and shear stress near the exit of the venturi. At that location in the counter-rotating case, strong shear stress is observed not only near the boundary of the central recirculation zone, as in the co-rotating case, but also near the tip of the prefilming surface (venturi). The latter is

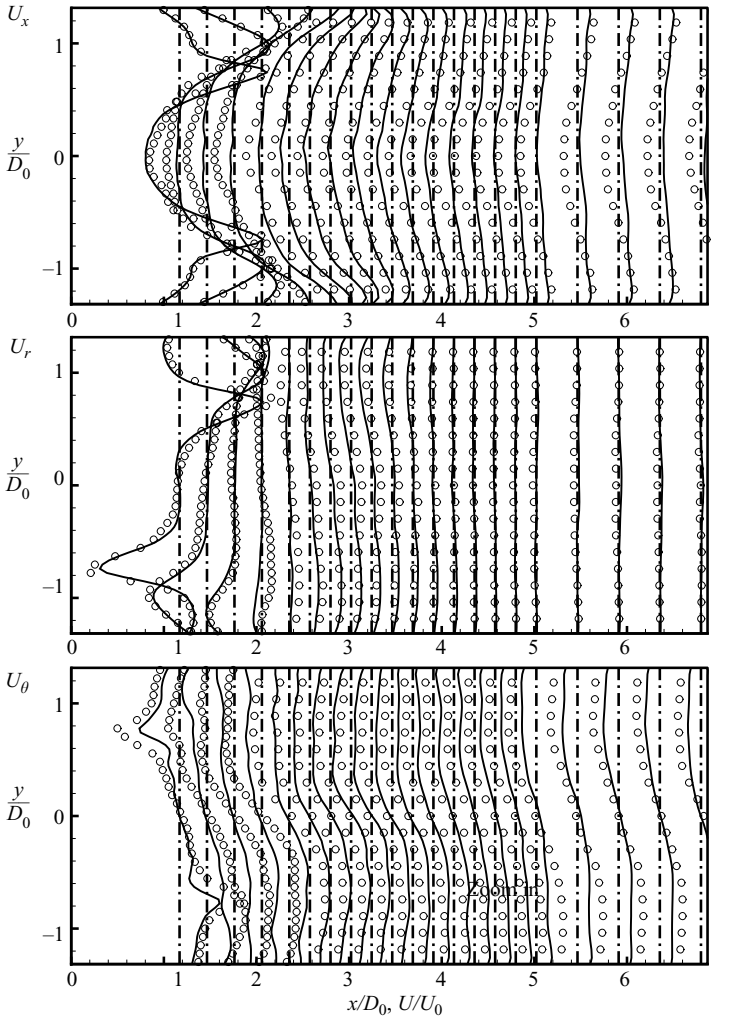

FIGURE 18. Radial distributions of normalized velocity components in axial, radial and azimuthal directions at various axial locations for co-(symbol) and counter-rotating (line) cases.

not observed in the co-rotating case. The co-rotating configuration also leads to the occurrence of PVC, which rotates and twists in the same direction as its counterpart in the counter-rotating case with a slightly lower frequency. The Strouhal number is 0.96 (1100 Hz). This common behaviour indicates that the key mechanisms dictating the primary flow dynamics in the two configurations are identical. The observation is further corroborated by the origin of the PVC being located upstream of the venturi, in which the flow motion is mainly controlled by the swirling flow through the primary swirler, as discussed previously.

A POD analysis of the co-rotating flow indicates that the standing acoustic wave inside the injector is significantly intensified. The energy carried by the two complementary modes of the vortex precession is only slightly higher than that of the standing acoustic wave.

In conclusion, the counter-rotating arrangement appears to be more desirable than its co-rotating counterpart for this particular injector design for several reasons. First,

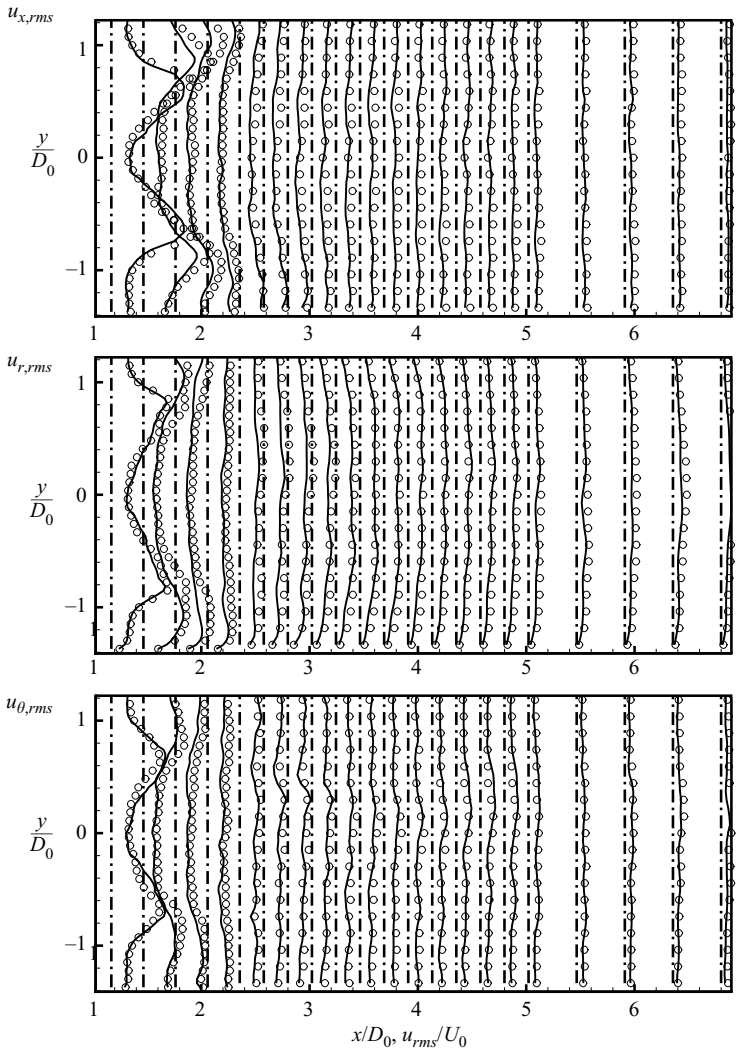

FIGURE 19. Radial distributions of normalized turbulent intensities in axial, radial and azimuthal directions at various axial locations for co-(symbol) and counter-rotating (line) cases.

the co-rotating configuration produces a longer central recirculation zone, which is more susceptible to flame oscillation (Huang & Yang 2004). Secondly, the strong shear layer and high-intensity turbulence near the trailing edge of the venturi in the counter-rotating case promote the development of the Kelvin–Helmholtz instability in the liquid film and subsequently facilitate the formation of fine droplets, as reported by Chin, Rizk & Razdan (2000). Thirdly, the counter-rotating flow accelerates the pressure recovery in the downstream region, and leads to a higher adverse pressure gradient along the axial axis. The resultant gradient further enhances the turbulent kinetic energy and vorticity downstream of the fuel nozzle, and facilitates the breakup of the liquid fuel. Therefore, the counter-rotating design is expected to produce finer droplets and a more stable flame.

6. Summary

A comprehensive numerical analysis has been conducted to investigate the turbulent swirling flow inside an operational gas-turbine injector with complex geometry. The formulation treats the unsteady three-dimensional conservation equations, with turbulence closure achieved using a large-eddy-simulation (LES) technique. Good agreement was obtained between the measured and calculated mean velocity fields and turbulence properties. The precessing vortex, which dominates the flow evolution in the swirl injector, was studied systematically. The twist direction of the spiral vortex core depends on the gradient of the angular velocity around the stagnation point. Both co- and counter-rotating inlet flow configurations were examined to evaluate the influence of the swirler orientation. The latter appears to be more effective in producing fuel/air mixtures for efficient and stable combustion because of the resultant shorter central recirculation zone and stronger shear stress and turbulence intensity in the region where the primary atomization of the liquid film occurs. The present work also demonstrated the feasibility of using LES to study complex flow fields in operational devices for engineering applications.

REFERENCES

Bazarov, V., Yang, V. & Puri, P. 2004 Design and dynamics of jet and swirl injectors. *Prog. Astronaut. Aeronaut.* **200**, 19–103.

Berkooz, G., Holmes, P. & Lumley, J. L. 1993 The proper orthogonal decomposition in the analysis of turbulent flows. *Annu. Rev. Fluid Mech.* **25**, 539–575.

Cai, J., Fu, Y., Elkady, A., Jeng, S. M. & Mongia, H. 2003 Swirl cup modeling part 4: effect of confinement. *AIAA Paper* 2003-0486.

Chin, J. S., Rizk, N. K. & Razdan, M. K. 2000 Effect of inner and outer airflow characteristics on high liquid pressure prefilming airblast atomization. *J. Propul. Power* **16**, 297–301.

Colin, O., Ducros, F., Veynante, D. & Poinsot, T. 2000 A thickened flame model for large eddy simulations of turbulent premixed combustion. *Phys. Fluids* **12**, 1843–1863.

Comte-Bellot, G. & Corrsin, S. 1971 Simple Eulerian time correlation of full- and narrow-band velocity signals in grid-generated, isotropic turbulence. *J. Fluid Mech.* **48**, 273–337.

Erlebacher, G., Hussaini, M. Y., Speziale, C. G. & Zang T. A. 1992 Toward the large eddy simulation of compressible turbulent flows. *J. Fluid Mech.* **238**, 155–185.

Germano, M., Piomelli, U., Moin, P. & Cabot, W. H. 1991 A dynamic subgrid-scale eddy viscosity model. *Phys. Fluids* A: *Fluid Dyn.* **3**, 1760–1765.

Grinstein, F. F., Young, T. R., Gutmark, E. J., Li, G. Q., Hsiao, G. & Mongia, H. C. 2002 Flow dynamics in a swirl combustor. *J. Turbulence* **3**, 030.

Gupta, A. K., Lilley, D. G. & Syred, N. 1984 *Swirl Flows*. Abacus, UK. Tunbridge Wells.

Hsiao, G. C. & Mongia, H. C. 2003 Swirl cup modeling part 3: grid independent solution with different turbulence models. *AIAA Paper* 2003-1349.

Hsiao, G. C., Mongia, H. C. & Vij, A. 2003 Swirl cup modeling part 2: inlet boundary conditions. *AIAA Paper* 2003-1350.

Hsieh, S. Y. & Yang, V. 1997 A preconditioned flux-differencing scheme for chemically reacting flows at all Mach numbers. *Intl J. Comput. Fluid Dyn.* **8**, 31–49.

Huang, Y. & Yang, V. 2004 Effect of swirl on combustion dynamics in lean-premixed swirl-stabilized combustor. *Proc. Combust. Inst.* **30**, 1775–1782.

Huang, Y., Sung, H. G., Hsieh, S. Y. & Yang, V. 2003 Large-eddy simulation of combustion dynamics of lean-premixed swirl-stabilized combustor. *J. Propul. Power* **19**, 782–794.

Huang, Y., Wang, S. W. & Yang, V. 2006 A system analysis of combustion dynamics in a lean-premixed swirl-stabilized combustor. *AIAA J.* **44**, 724–740.

James, S., Zhu J. & Anand, M. 2006 Large-eddy simulations as a design tool for gas turbine combustion systems. *AIAA J.* **44**, 674–686.

Kim, W. W., Menon, S. & Mongia, H. C. 1999 Numerical simulations of reacting flows in a gas turbine combustor. *CST* **143**, 25–62.

Lasheras, J. C. & Hopfinger, E. J. 2000 Liquid jet instability and atomization in a coaxial gas stream. *Annu. Rev. Fluid Mech.* **32**, 275–308.

Lefebvre, A. H. 1999 *Gas Turbine Combustion*, 2nd edn. Taylor & Francis.

Lu, X. Y., Wang, S. W., Sung, H. G., Hsieh, S. H. & Yang, V. 2005 Large-eddy simulation of turbulent swirling flows injected into a dump chamber. *J. Fluid Mech.* **527**, 171–195.

Lucca-Negro, O. & O'Doherty, T. 2001 Vortex breakdown: a review. *Prog. Energy Combust. Sci.* **27**, 431–481.

Manampathy, G., Mongia, H. C. & Jeng, S. M. 2003 Swirl cup modeling part 8: spray combustion in CFM56 single cup flame tube. *AIAA Paper* 2003-0319.

Martin, M. P., Piomelli, U. & Candler, G. V. 2000 Subgrid-scale models for compressible large-eddy simulations. *Theoret. Comput. Fluid Dyn.* **13**, 361–376.

Meneveau, C. & Katz, J. 2000 Scale-invariance and turbulence models for large-eddy simulation. *Annu. Rev. Fluid Mech.* **32**, 1–32.

Moin, P. 2002 Advances in large eddy simulation methodology for complex flows. *Intl. J. Heat Fluid Flow* **23**, 710–720.

Moin, P. 2004 Large eddy simulation of multi-phase turbulent flows in realistic combustors. *Prog. Comput. Fluid Dyn.* **4**, 237–240.

Moin, P. & Apte, S. 2006 Large-eddy simulation of realistic gas turbine combustors. *AIAA J.* **44**, 698–708.

Mongia, H. C. 1998 Aero-thermal design and analysis of gas turbine combustion systems: current status and future direction. *AIAA Paper* 1998-3982.

Mongia, H. C., Al-Roub, M., Danis, A. *et al.* 2001 Swirl cup modeling: part 1. *AIAA Paper* 2001-3576.

Mongia, H. C., Held, T. J., Hsiao, G. C. & Pandalai, R. P. 2003 Challenges and progress in controlling dynamics in gas turbine combustors. *J. Propul. Power* **19**, 822–829.

Novak, F. & Sarpkaya, T. 2000 Turbulent vortex breakdown at high Reynolds number. *AIAA J.* **38**. 287–296.

Piomelli, U. 1999 Large-eddy simulation: achievements and challenges. *Prog. Aero. Sci.* **35**, 335–362.

Piomelli, U., Moin, P. & Ferziger, J. H. 1988 Model consistency in large eddy simulation of turbulent channel flows. *Phys. Fluids* **31**, 1884–1891.

Pope, S. B. 2000 *Turbulent Flows*. Cambridge University Press.

Pope, S. B. 2004 Ten questions concerning the large-eddy simulation of turbulent flows. *New J. Phys.* **6**, 35.

Selle, L., Lartigue, G. Poinsot, T. *et al.* 2004 Compressible large eddy simulation of turbulent combustion in complex geometry on unstructured meshes. *Combust. Flame* **137**, 489–505.

Stevens, E. J., Held, T. J. & Mongia, H. 2003 Swirl cup modeling part 7: partially- premixed laminar flamelet model validation and simulation of single-cup combustor with gaseous *n*-heptane. *AIAA Paper* 2003-0488.

Syred, N. 2006 A review of oscillation mechanisms and the role of the precessing vortex core (pvc) in swirl combustion systems. *Prog. Energy Combust. Sci.* **32**, 93–161.

Syred, N. & Beer, J. M. 1972 The damping of precessing vortex cores by combustion in swirl generators. *Astron. Acta* **17**, 783–801.

Veynante, D. & Vervisch, L. 2002 Turbulent combustion modeling. *Prog. Energy Combust. Sci.* **28**, 193–226.

Wang, P., Bai, X. S., Wessman, M. & Klingmann, J. 2004 Large eddy simulation and experimental studies of a confined turbulent swirling flow. *Phys. Fluids* **16**, 3306–3324.

Wang, S. W., Hsieh, S. Y. & Yang, V. 2005 Unsteady flow evolution in swirl injector with radial entry, part i: stationary conditions. *Phys. Fluids* **17**, 045106.

Yoshizawa, A. 1986 Statistical theory for compressible turbulent shear flows, with the applications to subgrid modeling. *Phys. Fluids* **29**, 2152–2164.

Zang, T. A., Dahlburg, R. B. & Dahlburg, J. P. 1992 Direct and large-eddy simulations of three-dimensional compressible Navier–Stokes turbulence. *Phys. Fluids* A **2**, 127–140.